Effect of surface steps on chemical ordering in the subsurface of Cu(Au) solid solutions

Kuo Liu,[1,*] Siming Zhang [●],[2,*] Dongxiang Wu,[1] Langli Luo,[1,†] Xianhu Sun [●],[1] Xiaobo Chen,[1] Dmitri Zakharov,[3] Shaobo Cheng,[4] Yimei Zhu,[4] Judith C. Yang,[5] Guofeng Wang,[2,‡] and Guangwen Zhou [●][1,§]

[1]*Department of Mechanical Engineering and Materials Science and Engineering Program, State University of New York, Binghamton, New York 13902, USA*

[2]*Department of Mechanical Engineering and Materials Science, University of Pittsburgh, Pittsburgh, Pennsylvania 15261, USA*

[3]*Center for Functional Nanomaterials, Brookhaven National Laboratory, Upton, New York 11973, USA*

[4]*Department of Condensed Matter Physics and Materials Science, Brookhaven National Laboratory, Upton, New York, 11973, USA*

[5]*Department of Chemical and Petroleum Engineering, University of Pittsburgh, Pittsburgh, Pennsylvania 15261, USA*

Atomic steps are typically assumed to only influence surface phenomena of solids. In contrast, here we show, using *in situ* atomic-resolution electron microscopy observations and atomistic modeling, the pronounced effect from surface steps in inducing compositional and structural evolution in the subsurface of a Cu(Au) solid solution. We find that Au surface segregation results in a stacked sequence of Cu-Au ordered phases in the subsurface. The presence of a monatomic step at the surface induces the formation of an antiphase boundary that extends from the surface step to deeper layers by maintaining the same composition profile associated with each terrace. The bunching of surface steps induces chemical disordering of the Cu-Au ordered phases in the subsurface region of the bunched steps. These results demonstrate the instant propagation of surface dynamics of atomic steps into the subsurface region and can find broader applicability in utilizing surface defects to tune the composition and structure in the subsurface of alloys.

I. INTRODUCTION

Although phase diagrams delineating the thermodynamic conditions for phase stability in bulk alloys are well established, the composition and structure at an alloy surface usually differ from those of the bulk. This phenomenon, referred to as surface segregation, has received significant attention because it influences a variety of materials properties including adsorption, catalysis, oxidation/corrosion, wetting, friction/wear, adhesion, and electrical contact [1–5]. A microscopic understanding of the surface properties of multicomponent materials requires as a prerequisite atomic-scale understanding of surface segregation induced compositional and structural changes. Despite this importance, dynamically understanding the microscopic processes governing the onset, promotion, and termination of surface segregation has rarely attained, mainly due to experimental difficulties in atomically and simultaneously monitoring the dynamic spatial-temporal processes of structure and composition evolution in both the surface and subsurface regions.

Surface and subsurface are intrinsically coupled during a segregation process because of required atomic exchanges between the surface and subsurface regions [6–9]. Therefore,

segregation induced composition and structure dynamics at the outermost surface layers may propagate toward deeper atomic layers in the subsurface region. Insight into such surface-subsurface interplay is needed for understanding the fundamental features of segregation. Deconvoluting the surface and subsurface interplay has been a major challenge. Although surface-sensitive spectroscopic techniques such as Auger electron spectroscopy and photoemission spectroscopy are useful to investigate the composition in the near surface region, they are not structure sensitive and incapable of unambiguously differentiating between surface and subsurface. This is because the detected signal intensity is a temporal and spatial superposition of signals originating from several atomic layers, thus yielding an average composition across the probing depth. While other techniques such as ion scattering spectroscopy and low-energy electron diffraction are surface specific and can provide both surface composition and structure information when used complementarily, they lack spatial resolution and are prone to averaging errors. Scanning tunneling microscopy is one of the few techniques suitable to obtain site-selective quantitative information. However, besides the fact that STM results are difficult to interpret if there are more than two atomic species involved, it lacks the capability of resolving the structure in deeper atomic layers and cannot be used at elevated temperature which is often needed to drive segregation and reach equilibrium.

Moreover, the study of segregation phenomena has been mostly focused on well-defined single crystals [7,10]. However, even the surface of a single crystal is still far from being perfect, containing a large number of defects such as atomic steps. Atomic steps—a defect common to crystal

---

surfaces—are thought to have a strong influence on surface properties such as chemical reactivity and crystal growth because the reduced coordination at step sites facilitates bond breaking/making with foreign species [11–15]. The ability to predict surface dynamics under such nonequilibrium conditions is often compromised by the poor knowledge of the surface-subsurface interplay of surface segregation phenomena. Understanding segregation is further complicated by the presence of surface defects and surface-subsurface interplay at surface defect sites.

In contrast, transmission electron microscopy (TEM) is not subject to the aforementioned limitations by the traditional surface science tools and offers the opportunity to study segregation phenomena by providing precise information on the atomic scale for both the surface and subsurface regions. Particularly, TEM has advanced significantly in recent years and enables the time-resolved study of surface segregation by flowing a reducing gas in the sample area to prevent the surface from oxidation (thereby maintaining the surface cleanliness) while simultaneously probing atomic structural evolution from the outermost surface layer to deeper atomic layers. Here we describe dynamic, atomic-scale TEM observations of the segregation in a Cu(Au) solid solution. Through the use of *in situ* TEM to spatially and temporally resolve the dynamic interplay between surface segregation and compositional ordering in the subsurface of the Cu(Au) solid solution, here we report the pronounced effect of surface steps in inducing dramatic compositional and structural changes to the subsurface, resulting in the formation of antiphase boundaries or chemical disordering, depending on the terrace widths between adjacent steps. This phenomenon cannot be readily revealed because of the difficulty of unambiguously differentiating the surface and subsurface and their interactions at the defect sites.

II. EXPERIMENTAL AND COMPUTATIONAL DETAILS

Cu-20 at. % Au(100) single-crystal thin films were used for the *in situ* TEM experiments. The Cu-Au thin films were prepared by *e*-beam co-evaporation of Cu and Au, where the alloy composition was controlled by the evaporation rate of the two *e* guns. The $Cu_{20}Au_{80}$ (100) single-crystal thin films with a nominal thickness of ∼50 nm were deposited on the NaCl(100) substrate. The grown films were removed from the NaCl substrate by flotation in deionized water, washed, and mounted onto a TEM specimen holder. The films have good continuity over large areas with uniform distribution of Cu and Au. Quantitative analysis of the energy-dispersive x-ray spectra was performed to confirm the targeted composition of the as-prepared Cu-Au film by controlling the evaporation rate of the two electron guns. *In situ* TEM experiments were conducted using a dedicated environmental TEM equipped with an objective-lens aberration corrector. The as-loaded Cu-Au film was cleaned inside the TEM by annealing the film at ∼350 °C in H_2 atmosphere ($pH_2 = 1 \times 10^{-3}$ Torr) to remove any native oxide. The complete removal of the oxide and surface cleanliness was confirmed by electron diffraction and electron energy loss spectroscopy. At the same time, holes and tears with faceted edges can be formed in the thin film from the heating process. This is analogous to the cleavage

of crystals in vacuum. The freshly generated facets are atomically clean and ideal for cross-sectional TEM observations of Au segregation induced structural changes that occur in the surface and subsurface area. The dynamic observations of Au-segregation induced structural and composition evolution were performed by *in situ* TEM imaging in the cross-sectional view and in the presence of H_2 gas flow to ensure the surface cleanliness of the sample. To rule out any artifacts from electron beam irradiation affecting the *in situ* TEM results, the *e*-beam effect was carefully minimized by adjusting the imaging condition in one area and then moving to a neighboring, fresh area for high-resolution TEM (HRTEM) imaging. In addition, our TEM observations by blanking and unblanking the electron beam confirmed that the electron beam effect has a negligible effect on the observed Cu-Au ordering and surface dynamics of atomic steps. Notably, the *in situ* HRTEM imaging experiments were performed with thin film specimens at elevated temperature in the presence of gas flow, where significant atomic mobility and thermal drift can affect detrimentally the image contrast and resolution that can be achieved in practice. *Ex situ* high-angle annular dark-field scanning transmission electron microscopy (HAADF-STEM) was performed to complement the *in situ* HRTEM observations.

The density functional theory (DFT) calculations were performed using the Vienna *ab initio* simulation package (VASP) [16] with the projector augmented wave approach [17]. The generalized gradient approximation (GGA) with the Perdew-Burke-Ernzerhof (PBE) [18] exchange-correlation functional was used to evaluate the exchange-correlation energy, with the plane wave cutoff energy of 500 eV. A Monkhorst-Pack [19] *k*-point grid of $6 \times 6 \times 1$ was used for all surface slab calculations. A supercell approach was used to model the surfaces with a vacuum region of 12 Å in the direction normal to the surface, minimizing the interaction between periodic images. The slab model has 20 atomic layers, among which the bottom five layers are fixed at their bulk crystal determined positions and all the other atoms are allowed to fully relax their positions. All the structures were relaxed until the residual force acting on each atom was lower than 0.01 eV/Å. To compute the lattice constant of random solid solution of $Cu_{20}Au_{80}$, special quasirandom structures (SQSs) [20] were generated using the ATAT code [21]. In order to achieve enough randomness for the structure, a bulk supercell of 100 atoms (80 Cu atoms and 20 Au atoms) was used in this work. A Monkhorst-Pack [19] *k*-point grid of $3 \times 3 \times 4$ was used for this bulk calculation. The lattice constant was obtained as $a_0 = 3.769$ Å for random $Cu_{20}Au_{80}$ solid solution, which is in agreement with experimental value of $a_0 = 3.776$ Å [22].

III. RESULTS AND DISCUSSION

We first determine the Au-segregation profile for an atomically flat surface. Figure 1(a) shows a [001] zone-axis high-resolution TEM (HRTEM) image of a (100) surface of the $Cu_{20}Au_{80}$ at 350 °C and $pH_2 = 1 \times 10^{-3}$ Torr of H_2. The subsurface region (with a thickness of ∼3 nm) has well-developed superlattice contrast, indicating Au-enrichment induced chemical ordering. This is also consistent with the Cu-Au phase diagram of the stability of the ordered phases
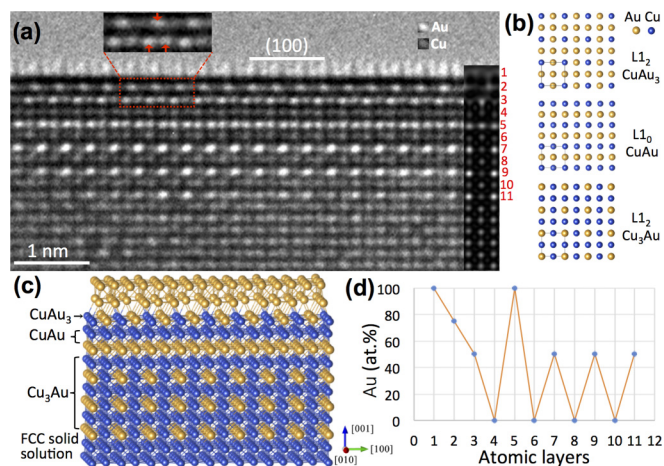
FIG. 1. Identification of the Au-segregation profile and compositional ordering in $Cu_{20}Au_{80}$ solution at $T = 350\,°C$ and $pH_2 = 1 \times 10^{-3}$ Torr. (a) HRTEM image of a (100) plane showing the formation of ordered phases in the subsurface. Upper inset: zoomed-in view of the area marked by the red rectangle. Right inset: simulated HRTEM image using the structure model in (c). (b) [010] projected views of Cu_3Au-$L1_2$, $CuAu$-$L1_0$, and $CuAu_3$-$L1_2$. (c) DFT-optimized structure. (d) Au-composition profile based on the stacking sequence of the ordered phases identified from (a)–(c).

up to $\sim390\,°C$ [23]. Based on the [001] projected views of the three Cu-Au ordered phases [Fig. 1(b)], the superlattice contrast from the 6th to 11th layers matches Cu_3Au-$L1_2$ while the contrast from the 4th to 5th layers is consistent with $CuAu$-$L1_0$. Similarly, the 3rd layer consists of alternate Au and Cu columns, but with the bright and faint contrast opposite to those in the 7th, 9th, and 11th layers of the Cu_3Au region, indicating the opposite packing sequence of Au and Cu atoms in the 3rd layer from Cu_3Au-$L1_2$. This is consistent with the difference in the packing of Au and Cu atoms in Cu_3Au and $CuAu_3$ [Fig. 1(b)], and the 3rd layer can thus be regarded as a single layer of $CuAu_3$-$L1_2$.

The 2nd layer shows significantly dimmed lattice contrast in alternate atom columns. The intensity of bright columns in the 2nd layer is almost the same as the bright ones in the 3rd layer. Consequently, the bright columns in the 2nd layer are assigned as pure Au. However, the overall intensity of the faint columns in the 2nd layer is much weaker than that of the corresponding columns in the 3rd layer, implying a composition difference. There are many possibilities about the composition of the dimmed columns in the 2nd layer. According to the analysis below, we assign the dimmed atom columns in the 2nd layer as the alternate presence of Au atoms and vacancies along the e-beam direction (i.e., 50 at.% Au and 50 at.% atomic vacancies). Based on the strong bright contrast of atom columns in the topmost layer and the trend of increasing Au concentration toward the surface, we assign pure Au atoms in the outmost surface layer. Although atomic columns in the topmost layer are resolved, the shape of the atom columns is slightly elongated, probably due to fast surface movement of Au atoms at elevated temperature. The atom columns in the 2nd layer are misaligned with the underlying lattice by half lattice spacing, as indicated by the red arrows in the inset zoom-in view in Fig. 1(a). This suggests that Au in the 2nd

layer is located at the bridge sites of underlying atoms in the 3rd layer instead of the normal face-centered cubic (fcc) hollow sites, resulting in the observed misalignment between the 2nd and 3rd layers. Au columns between the surface and 2nd layers are well aligned, indicating that Au atoms in the surface layer locate at the normal fcc hollow sites of the 2nd layer.

Comparisons between the experimental and simulated HRTEM images are used to identify the Cu-Au ordered phases formed from the interplay of Au segregation and compositional ordering. The HRTEM imaging shows the formation of Cu_3Au-$L1_2$, $CuAu$-$L1_0$, and $CuAu_3$-$L1_2$ with sequentially increasing Au concentration from inner layers toward the surface. Based on the experimental HRTEM observations shown in Fig. 1(a), we construct a structure model based on the above analysis and use density-functional theory (DFT) to obtain the minimum-energy structure [Fig. 1(c)]. The DFT-obtained minimum structure is then used to perform HRTEM simulations (see Supplemental Material Fig. S1 [24]) for direct comparison to the experimental HRTEM images. The intensity profiles of the atom columns taken along the different lines marked in Supplemental Material Figs. S2(a) and S2(d) are shown in Fig. S2(e)–S2(h) [24]. Intensity profiles of the simulated HRTEM image closely match those of the experimental HRTEM image. As shown in the inset of Fig. 1(a), the simulated image based on the DFT-optimized structure [Fig. 1(c)] reproduces the characteristic superlattice contrast and is broadly consistent with the experimental HRTEM image including intensity profiles along different lattice planes [24]. Figure 1(d) is the Au-composition profile based on the above structure analysis, having 100% of Au for the 1st and 5th layers and 50% of Au for the 2nd, 3rd, 7th, 9th, and 11th layers. It is worth mentioning that the H_2 gas has no influence on the observed segregation other than providing a reducing environment to maintain the surface cleanliness because of high dissociation barriers of H_2 molecules on Cu and Au surfaces [25,26]. Even for atomic H, it bonds weakly to Cu and Au, and desorbs from Au surfaces above $-163\,°C$ [27] and from Cu surfaces above $\sim22\,°C$ [28]. This is consistent with our ambient-pressure x-ray photoelectron measurements, showing no noticeable differences in the surface composition of $Cu_3Au(100)$ during annealing between ultrahigh vacuum and H_2 gas [29].

Figure 2 shows the dynamic interplay between surface migration of steps and structure evolution in the subsurface before reaching the equilibrium segregation (Fig. 1). Figires 2(a)–2(d) show the initial-stage segregation along with the motion of a monatomic step (see Supplemental Material *in situ* movie 1 [24]) where chemical ordering in the subsurface is still not fully developed. As marked by the yellow rectangle in the enlarged view of the red box [Fig. 2(a)], all the atom columns in the 4th layer of the subsurface region in front of the surface step show bright contrast, suggesting a pure Au layer in the marked region. This Au layer grows and propagates synchronously with the retraction motion of the step, and the atom columns evolves into alternate bright and faint contrast. This trend becomes more apparent upon further retraction of the step and the superlattice contrast in the same region becomes increasingly sharper with time [Fig. 2(c)], indicative of improved chemical order. The retraction motion of the step
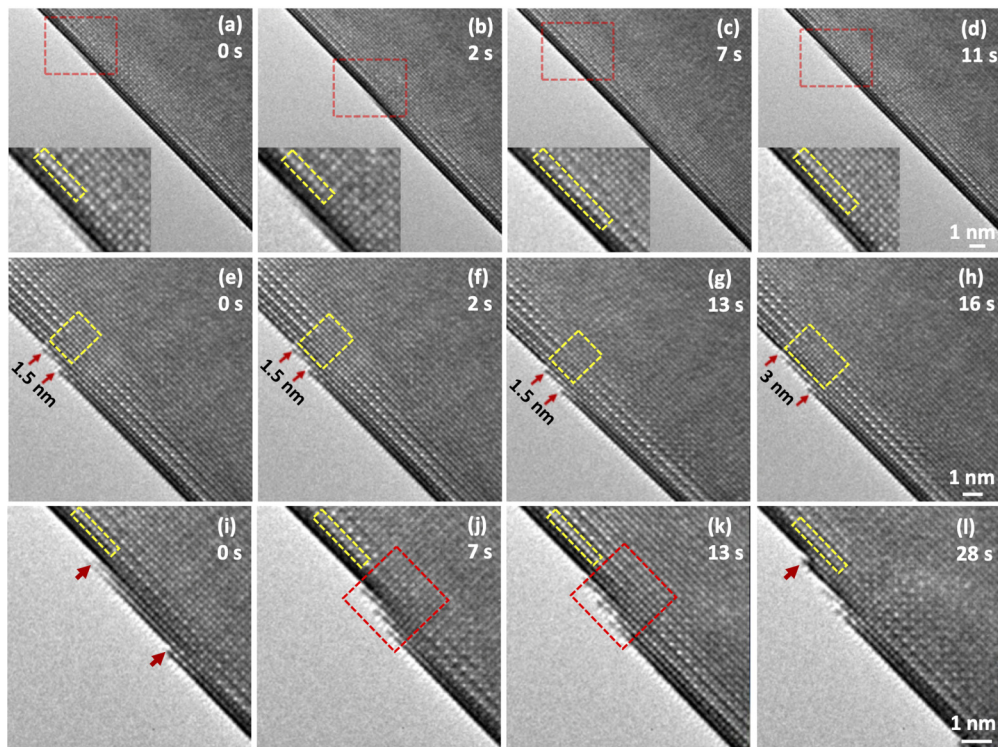
FIG. 2. *In situ* atomic-scale imaging of surface-step motion induced composition/structure evolution in the subsurface of Cu(Au) at $T = 350\,^{\circ}\text{C}$ and $pH_2 = 1 \times 10^{-3}$ Torr. (a)–(d) Migration of a monatomic step (Supplemental Material *in situ* TEM movie 1 [24]). The surface consists of two terraces separated by a monatomic step. Insets: enlarged view of the areas marked by dashed red boxes, the inset yellow rectangles mark the same atomic layer. (e)–(h) Migration of two bunched steps (Supplemental Material *in situ* TEM movie 2 [24]). The surface consists of three terraces separated by two monatomic steps. The yellow rectangles mark the subsurface region of the narrow terrace in the middle. The red arrows mark the two bunched steps. (i)–(l) Migration of three bunched steps (Supplemental Material *in situ* TEM movie 3 [24]). The surface consists of three terraces separated initially by a double-layer atomic step and one monatomic step, as indicated by the red arrows. The dashed red boxes mark the subsurface region of the bunched steps. The yellow rectangles mark the same atomic layer in the subsurface of the wide terrace.

is reversed to the forward motion by step-edge attachment of surface adatoms. Strikingly, this also reverts the ordered layer to a chemical disorder state, as evidenced by the observed transition from the superlattice contrast to the nearly uniform lattice contrast [marked by the yellow rectangles in Figs. 2(c) and 2(d)].

Figures 2(e)–2(h) show the subsurface evolution upon the surface motion of two bunched steps. The surface consists of two wide terraces separated by one narrow terrace bounded with two monatomic steps [Fig. 2(e)]. Initially, the subsurface region of the two wide terraces displays well-developed superlattice contrast, whereas the subsurface of the narrow terrace shows relatively uniform lattice contrast (the region marked by the yellow box). This indicates the strong tendency of chemical ordering in the subsurface of the wide terraces but disordering in the subsurface of the bunched steps. As seen from Supplemental Material *in situ* movie 2 [24] and Figs. 2(f)–2(h), the surface steps exhibit forward/backward motions as a result of attachment/detachment of atoms at the step edges, consistent with the modeling prediction of step motion with surface steps as both the sources and sinks of segregated adatoms and advacancies [30]. Surprisingly, this in turn induces the forward/backward motion of the ordered subsurface regions of the two wide terraces. Debunching of the steps results in the widening of the terrace in the middle

and correspondingly induces more ordering in the subsurface region of the terrace, as indicated by the improved superlattice contrast [Fig. 2(h)]. Our *in situ* observations indicate that the shrinkage in the terrace width to less than ~3 nm induces chemical disordering in the subsurface whereas widening the terrace width favors ordering in the subsurface of the terrace.

Figures 2(i)–2(l) illustrate another example of the step-bunching induced structure evolution in the subsurface (Supplemental Material *in situ* movie 3 [24]). The surface consists of three terraces separated by single and double-layer atomic steps [Fig. 2(i)]. In the beginning, the terrace in the middle is relatively wide, and the subsurface of all the three terraces is relatively ordered. The terrace shows retraction motion by atom detachment at the double-layer step, resulting in bunching of the three steps [Fig. 2(j)]. Correspondingly, the subsurface of the bunched steps exhibits the order → disorder transition, as indicated by significantly weakened superlattice contrast in the region marked by the red rectangle [Fig. 2(j)]. Meanwhile, the superlattice contrast in the layer marked by the yellow rectangle in Fig. 2(j) evolves into uniform bright contrast [Fig. 2(k)], indicative of its composition change to pure Au upon the retraction motion of the bunched steps. This process is reversed by de-bunching the steps and the terrace in the middle grows wider by the advancement of the surface step [Fig. 2(l)]. As a result, the atom columns marked by the
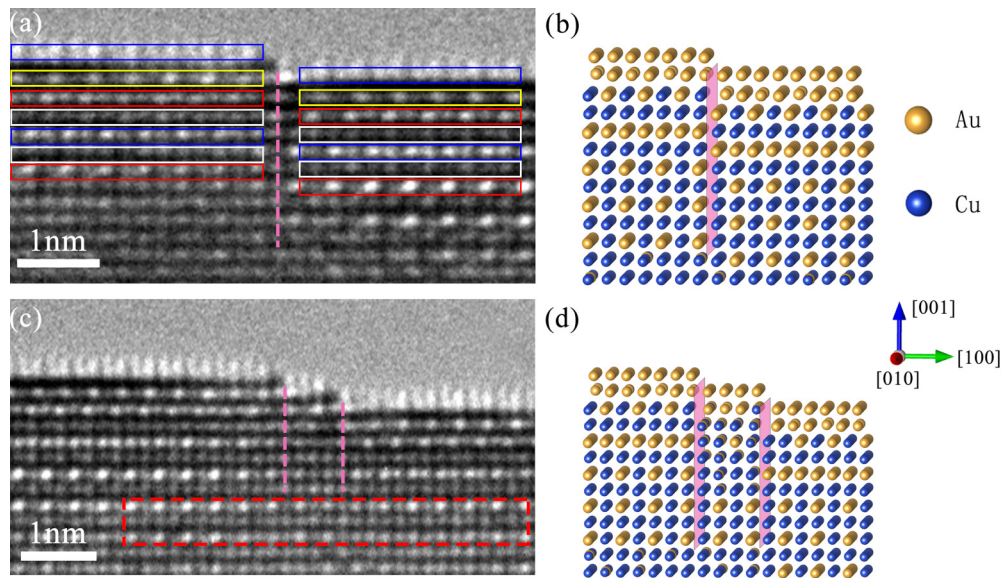
FIG. 3. Au segregation at stepped surfaces of the Cu(Au) at $T = 350\,^\circ$C and $p\text{H}_2 = 1 \times 10^{-3}$ Torr. (a) (100) surface consisting of a monatomic step. Atomic layers marked with the rectangles of the same color have the same phase and composition. The monatomic step results in antiphase boundary formation by the misalignment of the ordered phases in the subsurface of the two terraces. (b) 3D illustration of the atomic structure in (a). (c) (100) surface consisting of two wide terraces and one narrow terrace separated by two monatomic steps. The subsurface of the narrow terrace is denoted by the dashed lines. The dashed red rectangle shows that the deeper layers of the subsurface of all the three terraces exhibit the same Cu_3Au-$L1_2$ ordering. (d) Three-dimensional (3D) illustration of the atomic structure in (c).

yellow rectangle in Fig. 2(l) show the tendency to develop into the superlattice contrast again. Figure 2 also shows that the lattice contrast in the bulk (deeper from the subsurface) remains nearly unchanged throughout the observations, indicating that the effect from the surface-step motion propagates only into the subsurface by a thickness of ∼3 nm.

Figure 3 further illustrates the effect of surface steps on the Au-segregation profile after relatively prolonged annealing of the $\text{Cu}_{80}\text{Au}_{20}$ solid solution to approach the equilibrium. Figure 3(a) shows a surface consisting of two wide (100) terraces separated by a monoatomic step. The subsurface of the two terraces exhibits well-developed superlattice contrast. Atomic layers marked by the rectangles of different colors represent different ordered phases based on the characteristic superlattice contrast of Cu_3Au-$L1_2$, CuAu-$L1_0$, and CuAu_3-$L1_2$ (Fig. 1). The two terraces have the same Au composition profile as that in Fig. 1, as evidenced by the same stacking sequence of the different ordered phases in the subsurface of each terrace. Because of the monatomic step, the ordered Cu-Au phases in the subsurface of the two terraces also shifts by one atom spacing. This results in an antiphase boundary along which the different ordered phases in the subsurface region of the two terraces are shifted by the surface height of the atom step, as indicated by the purple line in Fig. 3(a) and the purple plane in Fig. 3(b).

Figure 3(c) shows a (100) surface consisting of two wide terraces and a narrow terrace in the middle, separated by two monatomic steps. This surface configuration resembles step bunching with significantly narrowed terrace widths in the bunched region. The subsurface of the two wide surface terraces shows the same stacking sequence of the ordered phases as that in Figs. 1 and 3(a). As indicated by the two purple lines in Fig. 3(c), the lattice contrast for the topmost seven atom

layers of the subsurface of the narrow surface terrace cannot be reliably assigned to any of the ordered phases, consistent with the step-bunching induced chemical disordering (Fig. 2). However, this step bunching effect dies out toward the deeper region [marked by the red rectangle in Fig. 3(c)], where the superlattice contrast of the entire region matches Cu_3Au-$L1_2$. Figure 3(d) shows the corresponding 3D illustration of the stepped surface in Fig. 3(c).

To further confirm the *in situ* HRTEM observations of the Au-segregation induced Cu-Au ordering, *ex situ* HAADF imaging was performed with the annealed Cu(Au) solid solution using aberration-corrected STEM. Figure 4(a) is a typical HAADF image showing the characteristic lattice feature of the Cu_3Au-$L1_2$ ordered structure in the relatively deep subsurface region as marked by the red box, where the bright and faint dots correspond to Au and Cu columns, respectively. This corroborates well with the *in situ* HRTEM observations in Figs. 1 and 3, showing the formation of the Cu_3Au-$L1_2$ ordered phase in the deeper layers. The ordering feature and segregation profile in the surface and near subsurface region is not well resolved in Fig. 4(a), which can be attributed to the electron beam effect from the STEM experiments with a condensed beam probe. The long acquisition time (8.5 s per frame) and higher probe current density required for STEM imaging resulted in some damage to the surface region (by knocking out atoms from the edge area). This is different from the HRTEM imaging mode in the *in situ* TEM observations, which had a more uniformly spread beam and faster frame rate (0.5 s per frame) to capture atomically resolved images of the surface dynamics. Figure 4(b) illustrates a HAADF image, showing the significantly weakened image contrast in the topmost layer due to the beam damage effect. However, it can still be resolved that the surface consists of two wide
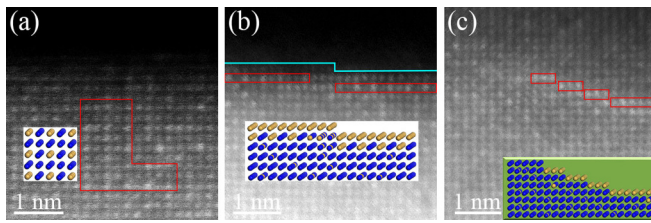
FIG. 4. *Ex situ* HAADF STEM micrographs of the Cu(Au) solid solution annealed at 350 °C in vacuum. (a) HAADF image illustrating the characteristic Cu_3Au-$L1_2$ ordering in the relatively deep atomic layers. (b) HAADF image showing the presence of two wide terraces separated by a monoatomic surface step (marked by the green line). The red rectangles mark the two atomic layers showing the $L1_2$ ordering of Cu and Au atoms in the subsurface region of the two terraces. The misalignment of the two atomic layers by one atom spacing along the monoatomic step direction indicates the tendency to form an antiphase boundary. (c) HAADF image showing the presence of surface ledges in a region far away from the sample edge, where the surface ledges are dominated by atom columns with brighter contrast, indicating the tendency to form pure Au atom columns along the ledges. The insets in (a)–(c) are the corresponding structure models of the regions marked by the red boxes.

terraces separated by a monoatomic step. As marked by the red rectangles, the alternate arrangement of bright and faint dots indicates the $L1_2$ ordering of Au and Cu atoms in the subsurface of the two terraces. The misalignment of the two

atomic layers by one atom spacing along the monoatomic step direction indicates the tendency to form an antiphase boundary, consistent with the *in situ* TEM imaging shown in Fig. 3(a). Figure 4(c) is a HAADF image obtained from a region that is relatively far away from the sample edge area, for which the atoms are less likely knocked out by the electron beam, and atoms along the ledges, therefore, can be imaged. As seen in Fig. 4(c), the atom columns along the surface ledges show brighter image contrast. This indicates that the outermost surface layer is indeed dominated by Au atoms, also consistent with the *in situ* HRTEM observations shown in Figs. 1–3.

Furthermore, DFT modeling was performed to elucidate the energetics of segregation profiles from the *in situ* TEM observations. Figure 5(a) shows the structure model with the identical stacking sequence of the Cu-Au ordered phases identified from our HRTEM observation (Fig. 1) along with ten bottom layers of $Cu_{20}Au_{80}$ fcc solid solution [24]. Specifically, the composition profile is composed of an outmost pure Au layer, one layer of ordered $CuAu_3$-$L1_2$, two layers of ordered $CuAu$-$L1_0$, and six layers of ordered Cu_3Au-$L1_2$. For comparison, we also constructed ten alternative composition profiles of the random $Cu_{20}Au_{80}$ solid solution (Fig. S3 [24]), as depicted in Fig. 5(b). All these structures are the slabs containing 20 layers of atoms and four atoms per layer. The total concentration of Au is 0.3 in all these structures, while the local composition profile is as follows: 1st layer 100% Au, 2nd–4th layers 50% Au, and 5th–10th layers
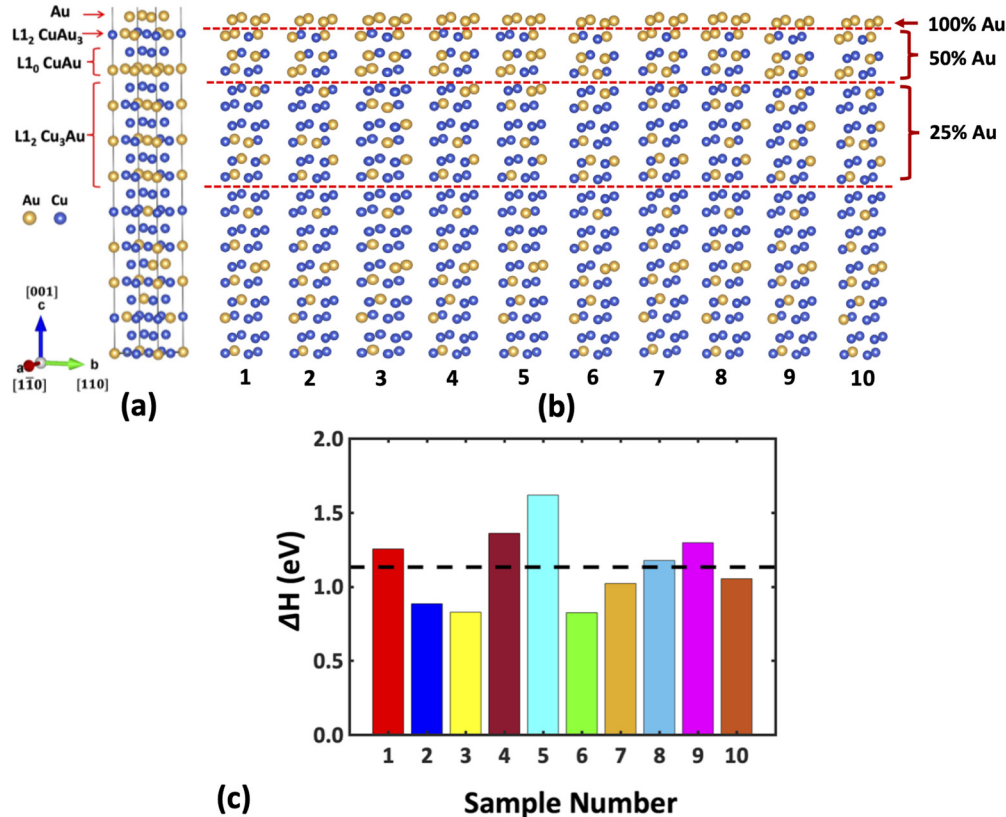

FIG. 5. (a) Atomic model of the (100) ordered segregation profile. (b) Ten alternative random solid solution models of the Cu-Au alloy. (c) DFT-computed relative enthalpies of ten alternative surface profiles of the random solid solutions in (b) with respect to the ordered segregation profile in (a).
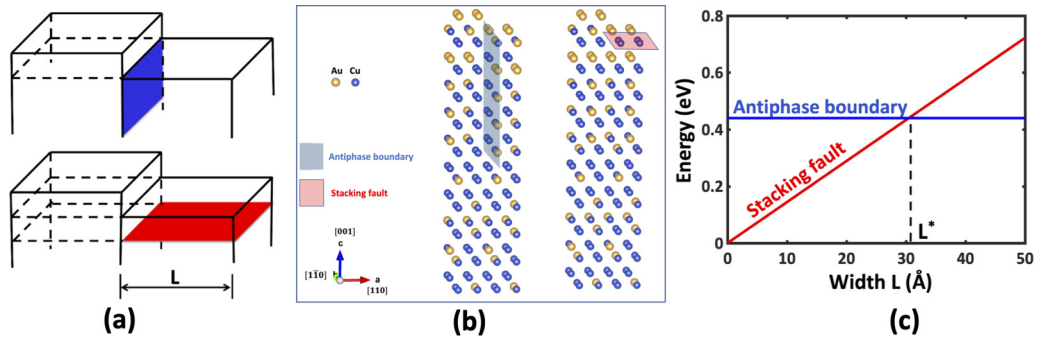
FIG. 6. (a) Schematic of the stepped surface with an antiphase boundary (colored in blue, top panel) and a stacking fault (colored in red, lower panel) in the subsurface. (b) Atomic models of the stepped surface with an antiphase boundary (blue parallelogram) beneath the monatomic step and the stepped surface with a subsurface stacking fault (red parallelogram) beneath the surface terrace. (c) DFT-calculated energies of the antiphase boundary and stacking fault as a function of the terrace width. Their intersection corresponds to the critical terrace width, beyond which the antiphase boundary formation is energetically more favored over the stacking fault.

25% Au. These composition values are identical with the ones of the experimentally observed stacking of the ordered structures in the subsurface [Fig. 5(a)], so the differences in enthalpy indicate their relative stability. It should be noted that modeling the full segregation profile shown in Figs. 1(c) and 1(d) is computationally challenging because of the large number of atoms needed for constructing the supercells consisting of multiple layers of the three Cu-Au ordered phases and the random Cu(Au) solid solution. Therefore, the second layer of pure Au in Fig. 1(c) is omitted in all the structure models of our DFT calculations. This omission of the pure Au layer does not change our conclusion because we only compare the relative stability of the segregation profile of the ordered Cu-Au phases with the alternative random Cu-Au solid solutions. Our DFT results [Fig. 4(c)] predict that the Au-segregation profile of Fig. 5(a) has a lower enthalpy than all the alternative profiles examined, in good agreement with our experimentally observed stacking sequence of the ordered phases. This is further confirmed by including the configurational entropy contribution, which has the form of $\Delta S = -R(X_{Cu} \ln X_{Cu} + X_{Au} \ln X_{Au})$, where X_{Cu} and X_{Au} are the mole fraction of Cu and Au in the alloy. Using the DFT calculated enthalpies shown in Fig. 5(c), it can be predicted that the Cu-Au ordering in Fig. 5(a) is stable against the alternative random solid solution profiles at temperature up to ~328 °C, which corroborates well with our experimental temperature of 350 °C.

We then illustrate the effect of surface steps on chemical ordering in the subsurface. As shown in Figs. 1–3, monatomic steps result in antiphase boundaries, along which the three ordered phases in the subsurface of adjacent wide terraces are shifted by the surface height of the step. We constructed two stepped surfaces consisting of two terraces and a monatomic step [Figs. 6(a) and 6(b)]. In one of the stepped structures, the two terraces are vertically shifted by one atomic layer to form an antiphase boundary in the subsurface. In the other structure, for comparison, a stacking fault is introduced to the second layer. In this way, there is no antiphase boundary between the ordered phases. Consequently, the energetics of the two stepped structures differs mainly between the antiphase boundary energy (E_{APB}) and stacking fault energy (E_{SF}). Figure 6(c) shows our DFT-computed energies of the antiphase

boundary and stacking fault, illustrating the relative stability of the two defects as a function of the terrace width L. The antiphase boundary energy is independent of L whereas the stacking fault energy increases linearly with L. For narrow terraces, the formation of stacking faults is dominant; for wide ones, the antiphase boundary formation becomes more favorable. Therefore, the critical terrace width L^* can be determined by balancing the antiphase boundary energy (E_{APB}) and the stacking fault energy (E_{SF}), as given in Eq. (1):

$$E_{APB} - E_{SF} \times L^* = 0. \qquad (1)$$

The E_{APB} and E_{SF} can be found by DFT calculations using the atomic structure models in Fig. 6(b). The calculated E_{APB} is 0.442 eV for an area of $\sqrt{2}a_0$ in length by $5a_0$ in height, where $a_0 = 3.769$ Å is lattice constant for this alloy, corresponding to the antiphase boundary structure in Fig. 6(b). The subsurface stacking fault energy is 14.5 meV/Å for the area of the same length $\sqrt{2}a_0$ with the unit terrace width for the stacking fault structure in Fig. 5(b). As shown in Fig. 5(c), L^* obtained from our DFT calculations is ~3.1 nm. This agrees well with our TEM observations, showing the formation of a stable antiphase boundary in the subsurface region of the stepped surface with terrace widths greater than ~3 nm [Fig. 3(a)]. By contrast, the subsurface of bunched steps is poorly ordered [Figs. 2(e)–2(l), and 3(c)]. This is attributed to the narrow terrace widths of the bunched steps, where the formation of less ordered structures (such as stacking faults) outcompetes with the extra energy costs for the formation of antiphase boundaries for the well-ordered phases.

It is worth mentioning that the observed minimum terrace width of 3 nm for the stabilization of the chemical ordering is not an occasional event in our experiments as it is confirmed by multiple observations at different places of the sample (Figs. 2 and 3). This is further confirmed by the good correspondence between the experimentally observed minimum terrace width for the stabilization of chemical ordering and the calculated critical terrace width for balancing the domain wall energy cost. It should also be borne in mind that the degree of chemical ordering depends on temperature [31–34], which in turn may affect the energy balance between an antiphase boundary and a stacking fault. Our energy balance model

can be employed to predict such a temperature effect on the minimum terrace width for the stabilization of the chemical ordering. This can be performed by first experimentally determining the chemical ordering behavior at a particular temperature of interest, based on which the energies of the corresponding antiphase boundaries and stacking faults can be computed by DFT. In this way, the minimum terrace width at the specific temperature can be predicted by substituting the DFT computed energies into Eq. (1).

Cu-Au is a model system for understanding surface segregation phenomena in alloys [32,35–43]. Most surface science studies were focused on stoichiometric intermetallic compounds of Cu-Au, for which the surface enrichment of Au is not significant because of the pairwise atomic interactions [10,32,35,36,44,45]. By contrast, here we dealt with the segregation in a Cu-Au solid solution alloy. The formation of a stack of CuAu$_3$-$L1_2$, CuAu-$L1_0$, and Cu$_3$Au-$L1_2$ ordered phases in the subsurface (Fig. 1) can be attributed to the strong interplay between surface segregation and chemical ordering [46–51]. The resulting Au-segregation profile [Fig. 1(d)] does not follow the monotonic oscillatory decay of Au in ordered Cu$_3$Au [10,36,44], indicating a significant difference in segregation between random solid solution and stoichiometric intermetallic alloys. Although step edges were shown to have stronger segregation than terraces [52–55], segregation, surface steps, antiphase boundaries, and chemical disordering are typically not considered together. Nevertheless, our results demonstrate that surface steps are a source of generating antiphase boundaries for the segregation-induced formation of ordered phases in the subsurface of the solid solution and inducing chemical disordering upon step bunching. Such phenomena have not been recognized due to the difficulty of probing the fast dynamics of the local atomic configurations in both surface and subsurface.

IV. CONCLUSIONS

In conclusion, we show the Au-segregation induced chemical ordering in the subsurface of random alloys. Different terraces of a stepped surface maintain the same composition profile with the antiphase boundary formation in the subsurface. However, step bunching induces chemical disordering in the subsurface of the bunched steps from the competing actions of antiphase boundaries and stacking faults. These results demonstrate the instant propagation of surface dynamics of atomic steps into the subsurface and are widely relevant as the partitioning of alloying elements to free surfaces and internal interfaces occurs in most multicomponent materials under suitable environmental bias.

[1] P. A. J. Bagot, K. Kruska, D. Haley, X. Carrier, E. Marceau, M. P. Moody, and G. D. W. Smith, J. Phys. Chem. C **118**, 26130 (2014).

[2] M. Gu, I. Belharouak, A. Genc, Z. Wang, D. Wang, K. Amine, F. Gao, G. W. Zhou, S. Thevuthasan, D. R. Baer, J. Liu, and C. Wang, Nano. Lett. **12**, 5186 (2012).

[3] R. Lin, E. Hu, M. Liu, Y. Wang, H. Cheng, J. Wu, J.-C. Zheng, Q. Wu, S. Bak, X. Tong, R. Zhang, W. Yang, K. A. Persson, X. Yu, X.-Q. Yang, and H. L. Xin, Nat. Commun. **10**, 1650 (2019).

[4] G. Pia, E. Sogne, A. Falqui, and F. Delogu, Sci. Rep. **8**, 15208 (2018).

[5] H. L. Xin, S. Alayoglu, R. Tao, A. Genc, C. M. Wang, L. Kovarik, E. A. Stach, L. W. Wang, M. Salmeron, G. A. Somorjai, and H. Zheng, Nano Lett. **14**, 3203 (2014).

[6] P. A. Dowben and A. Miller, *Surface Segregation Phenomena* (CRC, Boca Raton, 1990).

[7] M. Polak and L. Rubinovich, Surf. Sci. Rep. **38**, 127 (2000).

[8] L. Peng, E. Ringe, R. P. Van Duynec, and L. D. Marks, Phys. Chem. Chem. Phys. **17**, 27940 (2015).

[9] J. Li, G. F. Wang, and G. W. Zhou, Surf. Sci. **649**, 39 (2016).

[10] M. A. Vasiliev, J. Phys. D: Appl. Phys. **30**, 3037 (1997).

[11] B. Böller, K. M. Durner, and J. Wintterlin, Nat. Catal. **2**, 1027 (2019).

[12] M. Giesen, Prog. Surf. Sci. **68**, 1 (2001).

[13] B. L. M. Hendriksen, M. D. Ackermann, R. van Rijn, D. Stoltz, I. Popa, O. Balmes, A. Resta, D. Wermeille, R. Felici, S. Ferrer, and J. W. M. Frenken, Nat. Chem. **2**, 730 (2010).

[14] H.-C. Jeong and E. D. Williams, Surf. Sci. Rep. **34**, 171 (1999).

[15] J. Camarillo-Cisneros, W. Liu, and A. Tkatchenko, Phys. Rev. Lett. **115**, 086101 (2015).

[16] G. Kresse and J. Furthmuller, Phys. Rev. B **54**, 11169 (1996).

[17] G. Kresse and D. Joubert, Phys. Rev. B **59**, 1758 (1999).

[18] J. P. Perdew, K. Burke, and M. Ernzerhof, Phys. Rev. Lett. **77**, 3865 (1996).

[19] H. J. Monkhorst and J. D. Pack, Phys. Rev. B **13**, 5188 (1976).

[20] A. Zunger, S.-H. Wei, L. G. Ferreira, and J. E. Bernard, Phys. Rev. Lett. **65**, 353 (1990).

[21] A. van de Walle, P. Tiwary, M. de Jong, D. L. Olmsted, M. Asta, A. Dick, D. Shin, Y. Wan, L.-Q. Chen, and Z.-K. Liu, Calphad: Comput. Coupling Phase Diagr. Thermochem. **42**, 13 (2013).

[22] M. A. Spiridonov, S. S. Popel, A. S. Krylov, and M. M. Mizotin, J. Phys.: Conf. Ser. **98**, 012014 (2008).

[23] H. Okamoto, D. Chakrabarti, D. Laughlin, and T. Massalski, J. Phase Equilib. **8**, 454 (1987).

[24] See Supplemental Material at http://link.aps.org/supplemental/ 10.1103/PhysRevB.103.035401 for HRTEM image simulations, detail of DFT calculation, and *in situ* TEM movies, which include Refs. [19–22].

[25] J. Greeley and M. Mavrikakis, J. Phys. Chem. B **109**, 3460 (2005).

[26] B. Hammer and J. K. Norskov, Nature (London) **376**, 238 (1995).

[27] M. Pan, A. J. Brush, Z. D. Pozun, H. C. Ham, W.-Y. Yu, G. Henkelman, G. S. Hwang, and C. B. Mullins, Chem. Soc. Rev. **42**, 5002 (2013).

[28] K. Mudiyanselage, Y. Yang, F. M. Hoffmann, O. J. Furlong, J. Hrbek, M. G. White, P. Liu, and D. J. Stacchiola, J. Chem. Phys. **139**, 044712 (2013).

[29] C. R. Li, Q. Q. Liu, J. A. Boscoboinik, and G. W. Zhou, Phys. Chem. Chem. Phys. **22**, 3379 (2020).

[30] S. Kosolobov, Sci. Rep. **9**, 13428 (2019).

[31] I. Zasada, L. Rok, S. Mroz, and T. Rychtelska, J. Chem. Phys. **133**, 234706 (2010).

[32] D. H. Oh, H. J. Kang, K. H. Chae, C. N. Whang, B. V. King, D. J. O'Connorc, and D. W. Moon, Surf. Sci. **477**, L289 (2001).

[33] H. Dosch and H. Reichert, Acta Mater. **48**, 4387 (2000).

[34] I. Zasada, L. Wojtczak, and S. Mróz, J. Alloys Compd. **469**, 593 (2009).

[35] K. R. Mecke and S. Dietrich, Phys. Rev. B **52**, 2107 (1995).

[36] H. Reichert, P. J. Eng, H. Dosch, and I. K. Robinson, Phys. Rev. Lett. **74**, 2006 (1995).

[37] M. D. Moreira, J. Vac. Sci. Technol. B **30**, 051802 (2012).

[38] H. P. Fischer, J. Reinhard, W. Dieterich, and A. Majhofer, Europhys. Lett. **46**, 755 (1999).

[39] L. F. Zou, C. M. Yang, Y. K. Lei, D. Zakharov, J. M. K. Wiezorek, D. Su, Q. Y. Yin, J. Li, Z. Y. Liu, E. A. Stach, J. C. Yang, L. Qi, G. F. Wang, and G. W. Zhou, Nat. Mater. **17**, 56 (2018).

[40] L. F. Zou, J. Li, D. Zakharov, W. A. Saidi, E. A. Stach, and G. W. Zhou, J. Phys. Chem. Lett. **8**, 6035 (2017).

[41] M. Okada, Y. Tsuda, K. Oka, K. Kojima, W. A. Diño, A. Yoshigoe, and H. Kasai, Sci. Rep. **6**, 31101 (2016).

[42] L. Zou, P. Cao, Y. Lei, D. Zakharov, X. Sun, S. House, L. Luo, J. Li, Y. Yang, Q. Yin, X. Chen, C. Li, H. Qin, E. A. Stach, J. C. Yang, G. Wang, and G. W. Zhou, Nat. Commun. **11**, 3934 (2020).

[43] L. F. Zou, W. A. Saidi, Y. K. Lei, Z. Liu, J. Li, L. Li, Q. Zhu, D. Zakharov, E. A. Stach, J. C. Yang, G. F. Wang, and G. W. Zhou, Acta Mater. **154**, 220 (2018).

[44] T. M. Buck, G. H. Wheatley, and L. Marchut, Phys. Rev. Lett. **51**, 43 (1983).

[45] V. Kumar and K. H. Bennemann, Phys. Rev. Lett. **53**, 278 (1984).

[46] B. A. Front, B. Legrand, G. Tréglia, and C. Mottet, Surf. Sci. **679**, 128 (2019).

[47] W. Chen, P. Dalach, F. Schneider, and C. Wolverton, Langmuir **28**, 4683 (2012).

[48] A. Lopes, G. Treglia, C. Mottet, and B. Legrand, Phys. Rev. B **91**, 035407 (2015).

[49] A. Hizia, A. Front, M. Said, F. Berthierc, G. Tréglia, and C. Mottet, Surf. Sci. **700**, 121626 (2020).

[50] S. Pandey, R. J. Koch, G. Li, S. T. Misture, H. Wang, and S. R. Phillpot, J. Alloys Compd. **809**, 151615 (2019).

[51] Y. Zhang, G. Kresse, and C. Wolverton, Phys. Rev. Lett. **112**, 075502 (2014).

[52] B. Moest, P. Wouda, A. D. van der Gon, M. Langelaar, H. Brongersma, B. Nieuwenhuys, and D. Boerma, Surf. Sci. **473**, 159 (2001).

[53] B. Moest, S. Helfensteyn, P. Deurinck, M. Nelis, A. W. Denier van der Gon, H. H. Brongersma, C. Creemers, and B. E. Nieuwenhuys, Surf. Sci. **536**, 177 (2003).

[54] B. B. Maranville, M. Schuerman, and F. Hellman, Phys. Rev. B **73**, 104435 (2006).

[55] D. O. Bellisario, J. W. Han, H. L. Tierney, A. E. Baber, D. S. Sholl, and E. C. H. Sykes, J. Phys. Chem. C **113**, 12863 (2009).